

# EMMA: Extracting Multiple physical parameters from Multimodal Data

Farhat Shaikh    Ayan Banerjee    Sandeep Gupta  
IMPACT Lab, School of Computing & Augmented Intelligence (SCAI)  
Arizona State University, Tempe, AZ  
{fshaik12, abanerj3, Sandeep.Gupta}@asu.edu

## Abstract

We introduce *EMMA*, a physics-informed multimodal framework that recovers all identifiable dynamical parameters of a system directly from raw video, audio, and image-based time-series observations. Unlike prior video-only approaches that struggle with occluded states, hidden actuation inputs, or assumptions about known initial conditions and coordinate frames, *EMMA* performs joint inference of explicit parameters, implicit dynamical components, and calibration invariants within a unified continuous-time model. *EMMA* leverages a Liquid Time-Constant (LTC) network to learn latent dynamics from heterogeneous modalities while a physics-constrained loss enforces consistency with the governing differential equations. A unified feature pipeline enables consistent alignment across video trajectories, acoustic signatures, and chart-derived measurements, allowing *EMMA* to estimate parameters under forced, implicit, and multivariate dynamics without requiring segmentation masks, differentiable rendering, or specialized sensors. Across 100+ scenarios including five standard dynamical benchmarks (75 Delfys videos), real-world rover and quadrotor systems with hidden inputs, and simulation-chart case studies spanning biological and chaotic systems, *EMMA* delivers robust multi-parameter recovery and significantly outperforms existing single-modality and equation-discovery baselines. Our results establish *EMMA* as a general, scalable solution for physics-consistent model extraction from opportunistic multimodal data. Code and data are available at: <https://github.com/ImpactLabASU/EMMA-CVPR2026>

## 1. Introduction

Learning the dynamical parameters that govern real-world physical systems directly from multi-modal vision data is essential for constructing high-fidelity digital twins of autonomous platforms, such as drones and planetary rovers,

for testing, simulation, fault diagnosis, and safety-critical decision support [4, 20, 44]. This task is an instance of inverse modeling, where latent physical parameters must be inferred from observable trajectories [25, 43].

Recent efforts have explored estimating dynamical parameters solely from video [1, 18, 29, 30, 34], motivated by the fact that classical inverse modeling requires accurate measurements of all state variables, often necessitating intrusive or expensive onboard sensors. Vision-only approaches seek to bypass this requirement by inferring states from passive, widely available cameras [37]. However, we observe that video alone frequently occludes key state variables, especially when systems operate under unobserved forcing inputs. For instance, in a rover excursion sequence, video frames reveal wheel pose but not wheel-power commands, making correct kinematic inference ill-posed. Audio, in contrast, may encode these hidden inputs e.g., wheel rotation acoustics strongly correlate with motor speed, highlighting the need for multi-modal (audio-visual) dynamical parameter estimation [8, 9].

Even with multi-modal inputs, certain contributors to system behavior, such as frictional drag or terrain-dependent resistive forces remain unmeasured. These correspond to implicit dynamics, i.e., latent components of the governing equations that cannot be directly sensed but may still be observable through nonlinear dependencies among measured states [12, 24, 38]. Recovering such implicit terms is crucial for building physically faithful digital twins [2, 3, 5], yet remains largely unaddressed in existing vision-based equation-discovery pipelines [10, 18, 30].

Another challenge in extracting dynamical models from video is that many existing methods implicitly assume access to invariants such as initial conditions, coordinate-system origins, or fixed reference frames [26, 30, 34]. These assumptions rarely hold in real-world video, where camera pose, scene geometry, and the absolute coordinate origin are unknown. Therefore, a practical model-extraction system must not only recover the governing dynamical parameters but also calibrate these invariants jointly, ensuring that the recovered model is expressed in the correct physical coor-

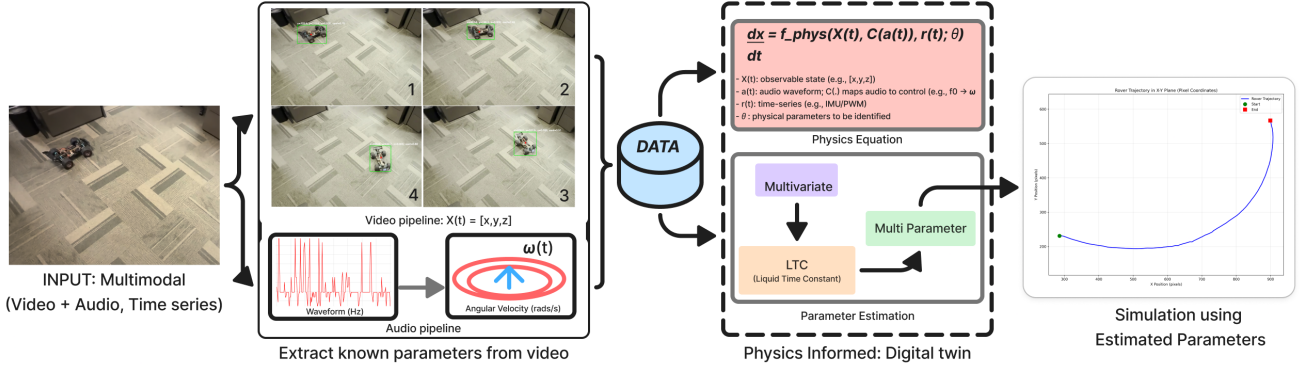


Figure 1. Given unified multi-modal observations (video, audio, image), EMMA extracts identifiable physical parameters through a physics-informed digital twin. The Liquid Time-Constant network learns dynamics in latent space while physics-constrained loss enforces consistency with governing equations. The estimated parameters enable accurate forward simulation without requiring frame reconstruction or segmentation masks.

dinate frame.

As summarized in Table 1, state of the art (SOTA) video-based dynamical parameter estimation methods typically (i) ignore external forcing inputs, (ii) recover only a single or limited subset of parameters, (iii) fail to handle implicit dynamical components, and (iv) assume access to known invariants such as initial conditions or coordinate origins.

In this paper, we introduce EMMA, a unified multi-modal audio-visual framework for dynamical parameter extraction that addresses all four limitations identified earlier. As shown in Fig. 1, EMMA ingests synchronized video, audio, and *auxiliary timeseries signals extracted from visual charts and figures* [35]. The video pipeline estimates observable states  $X(t)$  (e.g.,  $[x, y, z]$ ), while the audio pipeline recovers latent actuation inputs such as wheel angular velocity  $\omega(t)$  from acoustic signatures, resolving state occlusions created by unobserved forcing inputs. These signals are fused inside a physics-informed parameter estimator built on multivariate Liquid Time-Constant (LTC) dynamics, which simultaneously (1) recovers explicit physical parameters, (2) infers *implicit dynamical components* that do not appear directly in any sensing modality but influence motion through nonlinear interactions, and (3) performs *invariant calibration* by estimating unknown coordinate-frame origins and initial conditions directly from raw video. The recovered parameters are then used to simulate system trajectories, validating physical consistency as shown on the right side of Fig. 1. Together, these components enable robust model recovery in realistic, instrumentation-limited autonomous-system settings.

**Our main contributions are summarized below:**

- **Multi-modal dynamical parameter extraction:** A unified framework that estimates multiple dynamical parameters from video, audio, and *time-series reconstructed*

from visual charts and figures, as visualized in Fig. 1.

- **Recovery under unobserved forcing inputs:** A method for inferring latent actuation inputs such as wheel speed from audio when these inputs are occluded in video, enabling parameter estimation under hidden forcing.
- **Estimation of implicit dynamics:** A mechanism for identifying parameters of unmeasured or latent physical effects (e.g., frictional drag) that shape system behavior but are not directly observable in any modality.
- **Invariant calibration from raw video:** Joint estimation of dynamical parameters and coordinate-system invariants, eliminating assumptions about known initial conditions, camera world alignment, or fixed reference frames.
- **Extensive experimental validation:** Evaluation on the Delfys video benchmark (75 videos), new audio, visual rover and drone datasets, and parameter extraction from *visual charts*, establishing EMMA as a general-purpose multi-modal inverse modeling framework.

## 2. Related work

Table 1 shows a survey of all competing works that extract physical parameters from video. **Baselines.** We adopt Delfys [10] as the primary baseline because it most closely matches our problem setting: *unsupervised, video* recovery of physical parameters for known continuous-time ODEs. It is *decoder-free* avoiding frame prediction and therefore remains stable on real videos with intensity or scale variations giving good accuracy. Competing video physics methods differ substantially in scope: some rely on *differentiable rendering with known geometry or templates* (grad-Sim/rSim,  $\phi$ -SfT) [22, 26], others focus on *state or action estimation* rather than parameter identification (RISP) [34], or operate under *different supervision regimes* such as simulation trained models (Vid2Param) or setups with measured control inputs [1, 30]. Approaches like NIRPI and

Work	Forcing input (external $u(t)$ )	Multi-parameter ( $>3$ unknowns)	Multivariate dynamics	Implicit dynamics	Multi-modal input	Learnable Invariant knowledge	Comparators
Delfys [10]	✗	✗	✓	✗	✗	✗	Yes: Primary quantitative baseline.
NIRPI [18]	✗	✗	✓	✗	✗	✗	Yes: Quantitatively compared in results.
PAIG [21]	✓	✗	✓	✗	✗	✗	Yes: Quantitatively compared in results.
gradSim / rSim [22]	✓	✓	✓	✗	✗	✗	No
RISP [34]	✓	✗	✓	✗	✗	✗	No
$\phi$ -SFT [26]	✓	✓	✓	✗	✗	✗	No
Vid2Param [1]	✗	✗	✓	✗	✗	✗	No
Kandukuri [30]	✓	✗	✓	✗	✗	✗	No
EMMA ours	✓	✓	✓	✓	✓	✓	

Table 1. Comparison of related work on model recovery *from video*. ✓ = demonstrated; ✗ = not demonstrated.

PAIG address simpler, unforced systems with a small number of unknowns [18, 21]. For completeness, we also report general equation discovery frameworks PySINDy/SINDy-PI and PINNs which require a video to state or video to field front-end and are thus not video-native [7, 16, 24, 41]. Consequently, our head to head comparisons emphasize **Delfys** as the most faithful and directly comparable baseline to EMMA.

### 3. Method

In this section, we describe components of EMMA in detail.

#### 3.1. Problem Formulation

**Unified multi-modal inputs.** The input to EMMA can be video  $\{I_t\}_{t=1}^T$  with  $I_t \in \mathbb{R}^{3 \times H \times W}$  or audio  $\{A_t\}_{t=1}^T$  with  $A_t \in \mathbb{R}^{L_a}$ , or images of charts  $\{M\}$  with  $M \in \mathbb{R}^{3 \times H_m \times W_m}$  from sensors or cameras or a **time synchronized** combination of audio and video. **Our goal:** estimate identifiable physical parameters  $\theta \in \mathbb{R}^K$  governing system dynamics. A **Dynamical system** is represented as a set of  $D$  dimensional states  $\mathbf{x}(t) \in \mathbb{R}^D$  evolves via parametric ODEs:

$$\frac{d\mathbf{x}(t)}{dt} = f(\mathbf{x}(t), \mathbf{u}(t); \theta), \quad (1)$$

where  $\mathbf{u}(t)$  are exogenous inputs often not available (occluded) in visual modalities, and  $f$  encodes domain-specific physics.

**Invariants** are time-independent reference quantities  $\psi$ , such as coordinate-frame origins, camera-to-world alignment, and initial states, that parameterize the transformation  $X_{\text{world}} = g(X_{\text{obs}}; \psi)$ . Although they do not evolve with the dynamics, they must be jointly estimated to express the recovered model in a physically meaningful frame.

**Implicit dynamics.** We assume that only a subset of state variables  $\mathbf{x}$  can be measured denoted by a measurement matrix  $M$  which is a  $D \times D$  diagonal matrix with  $M(i, i) = 1(0)$  if the  $i^{\text{th}}$  state variable is measured (or not).

**Parameter estimation.** Given an estimated  $\theta_{est}$  and  $\mathbf{x}_0$ , we simulate Eq. 1 to obtain trajectory  $\mathbf{x}^{\text{sim}}(t)$  and observables

$\mathbf{y}_t^{\text{sim}} = P_{\text{obs}}(\mathbf{x}^{\text{sim}}(t))$ . We minimize:

$$\min_{\theta, \mathbf{x}_0} \frac{1}{T} \sum_{t=1}^T \|\mathbf{y}_t - \mathbf{y}_t^{\text{sim}}\|_2^2 + \mathcal{R}(\theta_{est}), \quad (2)$$

where  $\mathcal{R}$  enforces physical validity (positivity, bounds).

#### 3.2. Architecture Overview

EMMA consists of three stages (Figure 2): (i) **unified multi-modal feature extraction** from video, audio, and images producing time-aligned sequences  $\{\mathbf{x}(t)\}_{t=1}^T$  through modality-specific processing with temporal synchronization; (ii) **Liquid Time-Constant network** modeling continuous-time latent dynamics with input-dependent time constants, outputting hidden trajectories  $\mathbf{h}(t) \in \mathbb{R}^H$ , where  $H$  is the hidden state dimension; (iii) **multi-parameter estimation** via sequence-to-sequence prediction with temporal averaging, yielding  $\bar{\theta} \in \mathbb{R}^K$ , resulting in a digital twin validated through physics simulation.

#### 3.3. Unified Multi-modal Feature Extraction

Our unified framework processes heterogeneous modalities through specialized pipelines that produce temporally-aligned feature sequences.

**Video pipeline.** From frames  $\{I_t\}_{t=1}^T$ , we extract object trajectories through five stages. *Stage 1 (Detection):* YOLOv11 [23] detects bounding boxes with confidence threshold 0.85 (higher thresholds cause significant frame loss). *Stage 2 (Filtering):* Three-stage filtering computes centers, removes edge detections (10px threshold), enforces temporal stability. *Stage 3 (Smoothing):* Kalman filter [28] with state  $[x, y, v_x, v_y]$  reduces jitter. *Stage 4 (Transform):* For pendulum, pixel-to-angular conversion  $\theta = \arctan\left(\frac{y-y_p}{x-x_p}\right)$ ; for motion, calibrated transforms. *Stage 5 (Denoising):* Weighted moving average (window 10) smooths coordinates. Output: physical coordinates  $\mathbf{p}(t) \in \mathbb{R}^{d_v}$ . We also evaluate an unsupervised Farneback optical flow alternative that achieves comparable accuracy without any pretrained detector, confirming that EMMA’s

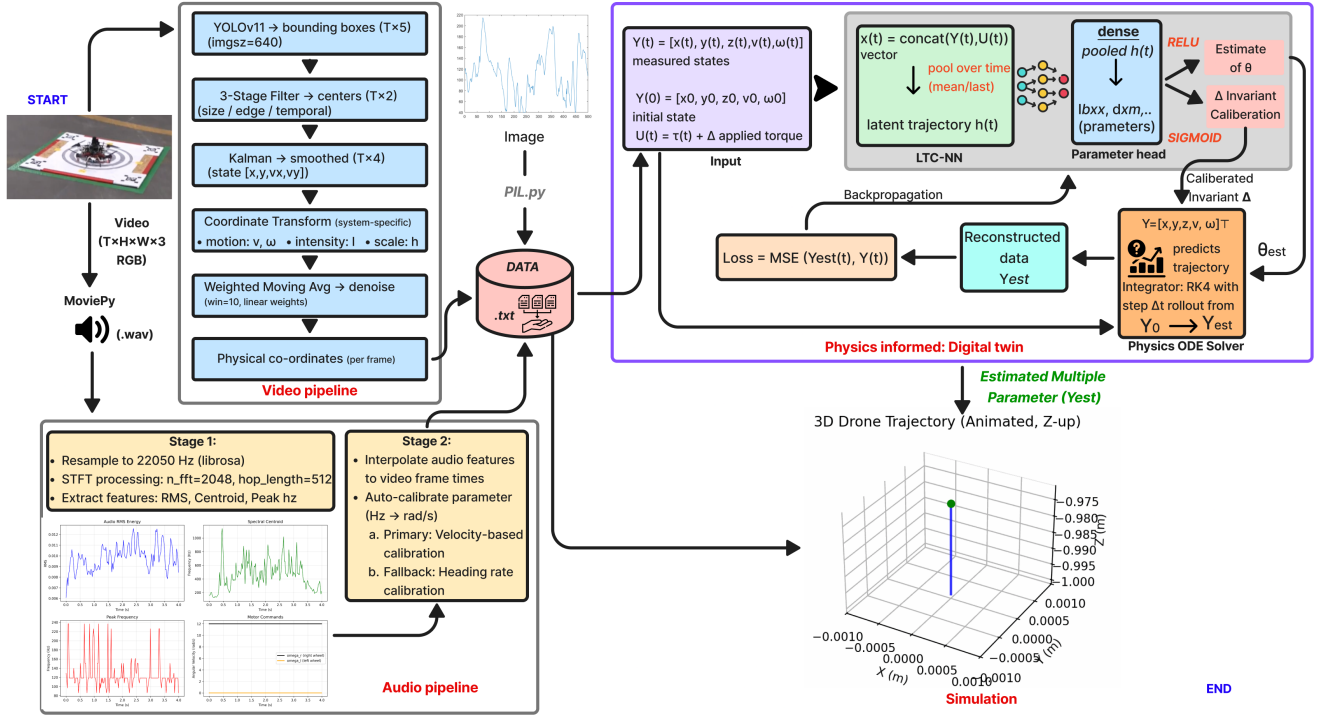


Figure 2. **EMMA Architecture.** Multi-modal inputs (video, audio and image) are processed through specialized pipelines into unified temporal representations. An LTC-NN learns latent dynamics  $h(t)$  and predicts physical parameters  $\theta$ . A differentiable physics simulator validates predictions, enabling end-to-end gradient flow. The framework successfully reconstructs digital twin drone (example shown) from multi-modal observations.

core contribution lies in the LTC physics layer rather than the specific feature extractor (see supplementary Table S4).

**Audio pipeline** has the following components:

a) *Signal processing:* Raw audio signals  $\{A_t\}_{t=1}^T$  are recorded at 44.1 kHz and resampled to 22.05 kHz. We compute the STFT (FFT size 2048, hop 512) using `librosa` [36], extracting RMS energy, spectral centroid, and dominant spectral peak frequency. All features are temporally aligned to video timestamps via an auto-calibration module, yielding acoustic feature vectors  $\mathbf{w}(t) \in \mathbb{R}^{d_a}$ .

b) *Datasheet-based linearity prior.* For non-flying rotors and rover wheels, manufacturer datasheets provide the nominal tonal frequency at a given RPM as well as the incremental change in frequency per unit increase in rotational speed. Empirically, the dominant tonal component of the acoustic signal varies approximately linearly with rotor/wheel speed in the non-flight regime. We therefore impose a linear audio-speed prior  $f_{\text{tone}}(t) \approx \alpha v(t) + \beta$ , where  $f_{\text{tone}}(t)$  is the extracted spectral peak frequency obtained from  $\mathbf{w}(t)$  and  $v(t)$  is the physical rotational speed. The affine transform parameters  $\alpha$  and  $\beta$  are calibration parameters (invariants) that are learned through the LTC-NN based component of EMMA.

**Image modality.** Images  $\{M_t\}_{t=1}^T$  from sensors, ther-

mal cameras, or measurement devices undergo feature extraction through CNNs or direct processing pipelines. For thermal imaging, we extract temperature distributions and gradients. For sensor images (e.g., medical scans, microscopy), we extract intensity profiles and spatial patterns. Output: image feature vectors  $\mathbf{m}(t) \in \mathbb{R}^{d_m}$ . We apply lightweight preprocessing with `Pillow` (PIL): load PNG or JPEG files, crop regions of interest, perform mode conversion (RGB to L and back), and normalize contrast before converting arrays to tensors. For chart images, we combine PIL pixel access with `OpenCV` masks to isolate the curve color and discretize it into  $(x, y)$  time series points for downstream modules.

**Unified temporal alignment.** All modality features undergo temporal interpolation to align with video frame timestamps, creating a unified temporal grid. Features concatenate to form multi-modal state vectors:

$$\mathbf{x}(t) = [\mathbf{p}(t); \mathbf{w}(t); \mathbf{m}(t)] \in \mathbb{R}^{D_{\text{in}}}, \quad (3)$$

where  $D_{\text{in}} = d_v + d_a + d_m$  depends on available modalities. Missing modalities are handled through zero-padding or learned embeddings.

**Spatial encoding for multimodal fusion.** For systems with multiple scenarios, temporal trajectories dis-

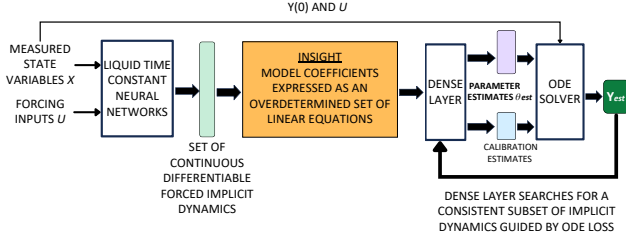


Figure 3. Intuition for using LTC-NN for parameter estimation.

cretized into  $N_{\text{spatial}} = 100$  samples per modality. This spatial encoding enables efficient processing of dense trajectory information while maintaining temporal coherence across heterogeneous inputs, producing unified representations  $\mathbf{x}_{\text{in}}(t) \in \mathbb{R}^{100}$ .

### 3.4. LTC Network for Continuous-Time Dynamics

The parameter estimation component of EMMA uses two fully connected layers (Figure 3): LTC-NN, which solves two problems of implicit dynamics and forcing inputs, and a dense layer that learns the model parameter estimates as nonlinear function of the LTC-NN hidden outputs and simultaneously calibrates the invariant estimates.

**How does LTC-NN tackle forcing inputs?** We use `ncps` library [17] with 64 hidden units. Each LTC-NN cell  $i$  implements:

$$\frac{dh_i}{dt} = \underbrace{\frac{-h_i}{1 + \tau_i f_{NN}(h_i, u, t, w_{NN})}}_{\text{models forcing inputs}} + \underbrace{f_{NN}(h_i, u, t, w_{NN})A}_{\text{models physics consistent dynamics}}, \quad (4)$$

where  $h_i(t) \in \mathbf{h}(t) \in \mathbb{R}^{64}$  is hidden state encoding latent dynamics across all modalities,  $\tau_i(t) > 0$  is a time constant [17] enabling adaptive response to multi-modal inputs,  $w_{NN}$  and  $A$  are recurrent weights,  $u(t)$  are inputs, and  $f_{NN}(\cdot, \cdot, \cdot, \cdot, \cdot)$  is the forward pass typically perceptron. Equation 4 shows that the forward pass of LTC-NN inherently has an input-dependent time constant that helps in modeling forcing inputs. We compare LTC against Neural ODE [11] and CT-GRU [15] in the supplementary (Table S7); under forcing inputs, LTC outperforms Neural ODE by 25% and CT-GRU by 5% in average parameter error, validating the importance of input-dependent time constants.

**How does LTC-NN model implicit dynamics?** The second part of Equation 4 is a set of hidden outputs that are themselves expressed as a consistent set of differential equations. These are much more variables than the required number of states in the system and hence carry the capability to model multiple implicit dynamics.

**How does EMMA obtain parameters?** The dense head in Fig. 3 maps measured and latent dynamics to physical parameters via a nonlinear readout with SIGMOID activations, leveraging the universal approximation property of

feedforward networks [13, 19]. This readout can be interpreted as a data-driven modal decomposition of latent trajectories, in the spirit of Dynamic Mode Decomposition and its Koopman extensions (EDMD) and variants with control (DMDc) [31, 40, 42, 45]. The predicted parameters are injected into the known ODE and the whole system is trained end-to-end via differentiable simulation, aligning with physics-informed and system-identification methodologies [7, 27, 41]. Because the SIGMOID range is  $(0, 1)$ , we apply the denormalization in Eq. (5).

**How does EMMA obtain calibration parameters?** For calibration, we add more cells in the dense layer than the number of dynamical parameters. These additional cells have RELU activation function and change linearly with hidden inputs and loss gradient. These hidden outputs are used for modeling the calibration parameters.

**Denormalization.** We map the dense layer outputs to physical scales via:

$$\theta_k = \left(1 + (0.5 - \bar{\theta}_k) \cdot \frac{95}{100}\right) \cdot \theta_k^{\text{nom}}. \quad (5)$$

### 3.5. Loss Functions and Training

**Physics-informed loss.** Total loss combines trajectory accuracy, calibration parameter along with constraints:

$$\mathcal{L}_{\text{total}} = \mathcal{L}_{\text{traj}}^{\text{cal}} + \lambda_{\text{param}} \mathcal{L}_{\text{param}}. \quad (6)$$

EMMA is *unsupervised* with respect to parameters: no ground-truth parameter values are used during training. Learning is driven solely by the physics-based loss (Eq. 6).

**Calibrated trajectory loss.** Measures discrepancy across measured variables:

$$\mathcal{L}_{\text{traj}}^{\text{cal}} = \sum_{i=1}^n M_{ii} \frac{1}{T_{\text{sim}}} \sum_{t=1}^{T_{\text{sim}}} \|x_i(t) - \gamma_i - x_{i,\text{sim}}(t)\|^2, \quad (7)$$

where  $\gamma_i$  is given by a dense layer RELU output if the  $i^{\text{th}}$  state variable requires calibration else  $\gamma_i = 0$ .

**Parameter constraints.** ReLU penalties enforce valid parameter ranges:

$$\mathcal{L}_{\text{param}} = \sum_{i=1}^{i=K} w_p(i) \text{ReLU}(-\theta_i) + w_l(i) \text{ReLU}(\theta_i - l_i) + w_{up}(i) \text{ReLU}(\theta_i - up_i), \quad (8)$$

where  $w_p$ ,  $w_l$ , and  $w_{up}$  are penalties for violating positivity, lower bound and upper bound respectively.

**Optimization.** AdamW [33] with cosine annealing [32], all parameters listed in Table 3.

**Implementation.** We implement EMMA in PyTorch [39] using the `ncps` library [17] for LTC networks with input size 100, 64 hidden units, sequence-to-sequence output, and 6 ODE unfolding steps. Video processing uses YOLOv11 [23] for detection and OpenCV [6] for tracking. Audio features are extracted with librosa [36] and MoviePy [47].

Method	Pendulum			Torricelli			Sliding Block			LED			Free Fall		
	$L$ [m]			$k$ [ $\sqrt{m}/s$ ]			$a$ [ $m/s^2$ ]			$\gamma$			$a$ [ $m/s^2$ ]		
	45cm	90cm	150cm	Small	Med	Large	Low	Med	High	Low	Med	High	Small	Med	Large
PAIG [21]	1.01 $\pm 0.03$	1.01 $\pm 0.04$	1.01 $\pm 0.04$	0.99 $\pm 0.01$	0.99 $\pm 0.01$	0.97 $\pm 0.02$	0.35 $\pm 0.03$	0.38 $\pm 0.02$	0.37 $\pm 0.04$	—	—	—	—	—	—
NIRPI [18]	0.77 $\pm 0.33$	0.84 $\pm 0.53$	0.63 $\pm 0.38$	0.21 $\pm 0.03$	0.14 $\pm 0.04$	0.16 $\pm 0.01$	-0.09 $\pm 0.88$	-0.01 $\pm 0.5$	-0.06 $\pm 0.01$	—	—	—	—	—	—
Delfys [10]	0.51 $\pm 0.01$	1.07 $\pm 0.2$	1.30 $\pm 0.02$	<b>0.0094</b> $\pm 4e^{-4}$	<b>0.0132</b> $\pm 5e^{-4}$	0.0167 $\pm 4e^{-4}$	1.29 $\pm 0.1$	2.70 $\pm 0.09$	3.44 $\pm 0.19$	2.24 $\pm 0.36$	0.97 $\pm 0.04$	0.41 $\pm 0.04$	15.0 $\pm 2.1$	9.51 $\pm 1.27$	<b>10.22</b> $\pm 1.21$
PySINDy [7]	0.28 $\pm 0.18$	0.77 $\pm 0.52$	1.24 $\pm 1.3$	0.035 $\pm 0.029$	0.027 $\pm 0.011$	0.068 $\pm 0.035$	2.13 $\pm 0.71$	2.64 $\pm 0.46$	2.63 $\pm 0.47$	1.74 $\pm 0.62$	0.73 $\pm 0.0$	0.37 $\pm 0.08$	2.64 $\pm 1.82$	6.66 $\pm 0.0$	1.50 $\pm 1.12$
EMMA	<b>0.50</b> $\pm 0.039$	<b>0.86</b> $\pm 0.073$	<b>1.50</b> $\pm 0.004$	0.0093 $\pm 0.0004$	<b>0.0132</b> $\pm 0.0008$	<b>0.0163</b> $\pm 0.0009$	<b>1.41</b> $\pm 0.018$	<b>2.27</b> $\pm 0.029$	<b>3.14</b> $\pm 0.050$	<b>2.29</b> $\pm 0.0$	<b>0.91</b> $\pm 0.0$	<b>0.45</b> $\pm 0.0$	<b>5.2</b> $\pm 1e^{-5}$	<b>9.95</b> $\pm 0.0$	10.29 $\pm 0.69$
GT	0.45	0.90	1.50	0.0095	0.0128	0.0162	1.441	2.300	3.141	2.3	0.92	0.46	9.8	9.8	9.8

Table 2. Comprehensive baseline comparison across multiple physical systems. EMMA demonstrates competitive or superior parameter estimation accuracy across motion-based dynamics (Pendulum, Torricelli, Sliding Block) and extends to non-motion domains (LED decay, Free Fall). Mean  $\pm$  standard deviation over five videos per configuration. Best results are in bold.

## 4. Evaluation

We have three evaluation objectives:

**Experiment A: Multi parameter study:** we test whether EMMA can accurately extract multiple parameters from video. **Benchmarks:** we use the Delfys [10] dataset for this experiment. We evaluate on five canonical physical systems with known ground-truth parameters. **Pendulum** dynamics estimate length  $L$  and damping coefficient  $\tau$  across three configurations (45cm, 90cm, 150cm) with 5 videos each. **Torricelli drainage** estimates the drainage constant  $k$  for three container sizes. **Sliding block** estimates acceleration and friction across three incline slopes. **LED decay** estimates decay rate  $\gamma$  across three temporal regimes. **Free fall** estimates gravitational acceleration  $g$  across three object sizes. Each configuration includes 5 videos, totaling 75 benchmark videos. Detailed information about the dynamical equations are provided in the supplementary documents. **Baselines:** We compare to video-based parameter inference methods PAIG [21], NIRPI [18], Delfys [10] for comparison with single parameter extraction and PySINDy [7] for multi-parameter extraction. **Metrics:** Since these examples have at most two parameters, we compare the raw values of the extracted parameters with standard deviation.

**b) Parameter extraction under implicit and forced dynamics,** we test whether EMMA can accurately extract parameters from multi-modal audio-visual data with implicit dynamics and forcing inputs for real world videos. **Benchmarks:** For real-world validation, we test on a differential-drive RC rover. It has 9 parameters including wheel radius, baseline width, and motor constants, while only 5 have known ground truths obtained from datasheets. We also utilize a 6-DoF quadcopter with 12 parameters out of which 7 are known. The rover video is collected in our lab, while the quadcopter video is collected from the lab Youtube page of University of Pennsylvania with ground

truth obtained from datasheets. Detailed information about ground truth information and datasheet are provided in supplement. **Baselines:** Since this is the first work to perform parameter extraction from multi-modal audio video data under forced inputs and implicit dynamics, there are no baselines for this task. We compare the extracted parameters with ground truth. **Metrics:** Raw values are compared with ground truth.

**c) Parameter extraction from charts of simulations,** we test whether EMMA can extract multiple known parameters from simulation chart images. These experiments demonstrate that EMMA can extract models from at least three different modalities. **Benchmarks:** We use the figures generated from the simulator available for each of the case studies reported in [16, 27]. There are four case studies of F8 Crusader, Lotka Volterra, Lorenz oscillator and HIV therapy. The exact image generation mechanism and the detailed dynamics is discussed in supplement. In addition we use a medical case study of automated insulin delivery system for Type 1 Diabetes. The data for this purpose was generated using the UVA/PADOVA Type 1 Diabetes Simulator [14]. The underlying dynamics is governed by Bergman Minimal Model with only sensed variable is glucose and all other variables are implicit. **Baselines:** PySindy is the main comparator in this case. However, since PySindy does not have a image pipeline, we use the EMMA image processing pipeline for both the evaluations of EMMA and PySindy ensuring fair comparison. **Metrics:** Since the number of parameters extracted are many and different for each application, for consideration of space we only report the root mean square error (RMSE) in reconstruction  $x_{rmse}$  of the data from learned parameters and the RMSE in parameter estimation  $\theta_{rmse}$ .

**Inputs and preprocessing.** EMMA accepts any subset of video, audio, and sensor modalities. Video processing em-

Parameter	Value
<i>LTC Network</i>	
Units, ODE unfolds, $\epsilon$	64, 6, $10^{-8}$
<i>AdamW Optimizer</i>	
$\eta, \lambda_{wd}, \epsilon, \beta_1, \beta_2$	$5 \times 10^{-3}, 10^{-4}, 10^{-8}, 0.9, 0.999$
<i>Cosine Schedule</i>	
$T_0, T_{mult}, \eta_{min}$	10, 2, $10^{-6}$
<i>Training</i>	
Window ( $T$ ), Stride, Batch, Patience, $p_{drop}$	16, 1, 32, 40 epochs, 0.3

Table 3. Training hyperparameters and configuration.

employs YOLOv11 for object detection (confidence threshold 0.85, image size 640 pixels), followed by Kalman filtering with state vector  $[x, y, v_x, v_y]$  and pixel-to-metric calibration via domain-specific coordinate transformations. Audio extraction uses MoviePy at 44,100 Hz with librosa spectral features (RMS energy, spectral centroid, peak frequency). All inputs undergo z-score normalization using training statistics; parameters are denormalized at inference via Eq. (5).

**Reporting and splits.** For each benchmark configuration, we compute mean  $\pm$  standard deviation over 5 videos. When sensors or audio are absent, we report results using available modalities. We fix random seeds and document all hyperparameters for reproducibility as detailed in Table 3. Multi-seed statistical validation (5 seeds) is provided in supplementary Tables S5 and S6 for rover and drone respectively.

## 4.1. Benchmark Results

**Experiment A: Single + Multi-parameter study on Video only:** Table 2 summarizes results across the five benchmark systems for single parameter estimation. EMMA achieves competitive or superior parameter accuracy. Relative to video baselines and PySINDY, EMMA consistently reduces parameter error.

*Pendulum:* EMMA recovers length  $L$  and damping  $\tau$  close to ground truth across 45/90/150 cm configurations. Video baselines show larger bias in  $L$  at extreme lengths. PySINDY’s derivative estimation is sensitive to noise and occlusion, producing parameter estimates with high variance.

*Torricelli:* EMMA accurately estimates the drainage constant  $k$  despite the  $\sqrt{h}$  nonlinearity. PySINDY method struggles to represent fractional powers, leading to systematic errors. Our physics-constrained loss stabilizes learning and tightly matches ground truth across container sizes with low variance ( $\pm 0.0004$  to  $\pm 0.0009$ ).

*Sliding block:* EMMA improves estimation of acceleration and friction across low, medium, and high slopes, producing lower error than video baselines and PySINDY. Parameter estimates remain stable across different slope configurations.

*LED decay:* EMMA closely matches decay rates across fast, medium, and slow regimes with low variance across videos. Error remains stable under moderate measurement noise, demonstrating robustness to realistic lighting variations and camera auto-adjustment artifacts.

*Free fall:* EMMA recovers gravitational acceleration  $g$  across object sizes and operating conditions. PySINDY baseline is sensitive to discrete differentiation and frame-rate variations, resulting in larger errors. EMMA’s continuous-time formulation via LTC networks handles irregular sampling naturally.

*Multi-parameter Settings:* Table 4 (a and b) shows the performance of EMMA in extracting multiple parameters from the benchmark examples available in the Delfys dataset. The only comparator here is PySINDY and EMMA is superior in estimating parameters.

*Takeaways:* Across five benchmarks spanning diverse physical regimes, EMMA’s physics-informed training and continuous-time dynamics deliver accurate parameter estimates. The framework outperforms baseline methods in most settings while eliminating mask requirements and pixel-space reconstruction overhead. Quantitative results with mean  $\pm$  std by configuration are shown in Table 2. EMMA could learn invariant parameters such as hanging point of the pendulum or pendulum starting point and did not use these as prior information. EMMA also converges accurately under expanded initialization bounds (200% range) in 5 of 6 configurations, confirming robustness to poor initialization (supplementary Table S8).

**Experiment B: Multi parameter extraction under implicit and forced dynamics:** Table 4 (c and d) shows the dynamical parameters estimated by EMMA and compares with the ground truth parameters in the two real world case studies of drone and rover. We could only compare EMMA estimated parameters with the available ground truths. EMMA has an average error of  $15.9\% \pm 7.4\%$  in estimating all measurable parameters of the drone, while it has  $8.8\% \pm 1.7\%$  for the rover example. For the Rover the center of mass (CoM) height and the wheel radius are parameters related to implicit dynamics, while for the drone example the thrust coefficient, torque coefficient, motor gain and motor time constant are implicit dynamics parameters. EMMA’s performance remained stable across parameters related to implicit or measured parameters.

*Takeaways:* Even under forcing inputs from the rover or drone controller, EMMA could extract parameters related to both measured and implicit dynamics. EMMA also performed good calibration since it did not use idle wheel power or quadrotor idle rotational speed as inputs or coordinate space origin as input instead EMMA learned the most appropriate invariants. Audio noise robustness experiments (supplementary Table S9) confirm that injecting Gaussian noise at SNR levels down to 5 dB causes less than 1.1%

(a) Pendulum							(b) Sliding Block						
Length	EMMA		PySINDy		GT		Slope	EMMA		PySINDy		GT	
	$L$ (m)	$\tau$ (1/s)	$L$ (m)	$\tau$ (1/s)	$L$ (m)	$\tau$ (1/s)		$\alpha$ ( $^\circ$ )	$\mu$	$\alpha$ ( $^\circ$ )	$\mu$	$\alpha$ ( $^\circ$ )	$\mu$
45cm	$0.507 \pm 0.039$	$0.055 \pm 0.026$	$0.36 \pm 0.06$	$0.73 \pm 0.57$	0.45	0.05	Low	$19.92 \pm 0.20$	$0.208 \pm 0.003$	$24.00 \pm 4.18$	$0.21 \pm 0.00$	20.0	0.20
90cm	$0.859 \pm 0.073$	$0.045 \pm 0.011$	$0.81 \pm 0.04$	$0.01 \pm 0.03$	0.9	0.05	Medium	$24.72 \pm 0.38$	$0.205 \pm 0.004$	$27.00 \pm 2.74$	$0.21 \pm 0.00$	25.0	0.20
150cm	$1.501 \pm 0.004$	$0.050 \pm 0.001$	$1.51 \pm 0.11$	$0.00 \pm 0.00$	1.5	0.05	High	$29.81 \pm 0.42$	$0.204 \pm 0.004$	$27.00 \pm 2.74$	$0.21 \pm 0.00$	30.0	0.20

(c) Rover (5 parameters)				(d) Drone (7 parameters)			
Parameter	Ground Truth	Value	Description	Parameter	Ground Truth	Value	Description
$a$	0.178 m	0.196 m	X-arm length	$k_{Th}$	1.1	1.017	Thrust coef.
$b$	0.144 m	0.134 m	Y-arm length	$k_{To}$	1.3	1.501	Torque coef.
$r$	0.201 m	0.223 m	Wheel radius	$k_p$	0.91	1.007	Motor gain
$m$	26.88 kg	24.44 kg	Mass	$\tau_2$	0.012	0.015	Motor time const.
$CM$	0.112 m	0.120 m	CoM height	$d_{xm}$	0.18	0.158	X-arm length
				$d_{ym}$	0.20	0.173	Y-arm length
				$d_{zm}$	0.07	0.051	Z-arm offset

Table 4. (4.a, 4.b) Side-by-side comparison of EMMA and PySINDy parameter estimates across shared physical systems. Values are mean  $\pm$  standard deviation over five videos. (4.c, 4.d) Rover and drone parameters estimated by EMMA, compared against ground truth (GT).

Example		EMMA		PySINDY	
		Implicit	Explicit	Implicit	Explicit
Lotka	$\theta_{rmse}$	$0.054 \pm 0.003$	$0.048 \pm 0.003$	$6.3 \pm 1.7$	$0.054 \pm 0.013$
Volterra	$x_{rmse}$	$0.03 \pm 0.009$	$0.03 \pm 0.005$	$12.7 \pm 2.4$	$0.05 \pm 0.01$
Chaotic	$\theta_{rmse}$	$0.016 \pm 0.005$	$0.015 \pm 0.005$	$2.3 \pm 0.5$	$0.022 \pm 0.009$
Lorenz	$x_{rmse}$	$1.7 \pm 0.4$	$1.68 \pm 0.4$	$37.4 \pm 6.1$	$3.66 \pm 1.1$
F8	$\theta_{rmse}$	$7.81 \pm 1.2$	$6.8 \pm 1.7$	$21.9 \pm 4.2$	$10.5 \pm 1.4$
Crusader	$x_{rmse}$	$1.6 \pm 0.3$	$1.57 \pm 0.3$	$35.2 \pm 7.3$	$3.46 \pm 0.9$
HIV	$\theta_{rmse}$	$0.45 \pm 0.11$	$0.39 \pm 0.09$	$4.5 \pm 0.9$	$0.43 \pm 0.1$
therapy	$x_{rmse}$	$28.9 \pm 4.7$	$28.3 \pm 3.2$	$89.1 \pm 12.7$	$28.8 \pm 2.7$
AID	$\theta_{rmse}$	$0.51 \pm 0.12$	$0.13 \pm 0.04$	$6.5 \pm 1.5$	$0.73 \pm 0.2$
therapy	$x_{rmse}$	$8.7 \pm 1.6$	$4.3 \pm 1.7$	$79.6 \pm 21.3$	$31.2 \pm 6.1$

Table 5. Multi-Parameter extraction from simulation charts. Comparison with and without implicit dynamics

variation in all estimated rover parameters.

**Experiment C: Parameter extraction from simulation charts:** In this experiment for the simulation charts we executed EMMA and PySINDY under two conditions: a) implicit dynamics, where the image pipeline was applied on only the chart of one state variable, hence only one state variable was measured while all others were unmeasured, and b) explicit dynamics, where the image pipeline was applied on charts of all state variables resulting in all measurable state variables. Table 5 compares the performance of EMMA and PySINDY. It shows while EMMA outperforms PySINDY on the parameter estimation task from charts, both EMMA and PySINDY performance decreases when the dynamics becomes implicit. However, EMMA has much less performance degradation than PySINDY.

## 4.2. EMMA Execution Time

Table 6 compares the execution time of EMMA with the next best performing comparator, Delfys [10]. EMMA takes  $1.4 \times$  more time than Delfys on an NVIDIA RTX Ada 6000 GPU. This is because the LTC-NN requires solution of ordinary differential equation and is an inherently more computationally heavy operation. This overhead is offset by

Model	Avg Time/Epoch (s)	Std. Dev. (s)	Parameters
Delfys (Baseline)	0.19	0.03	5.7M
EMMA (Ours)	0.37	0.01	53.2K

Table 6. Training efficiency comparison between Delfys [10] and EMMA.

EMMA’s novel capabilities (multi-parameter, forced, and implicit dynamics estimation) and its  $107 \times$  smaller model size. EMMA’s compact size also suits edge deployment; related model recovery architectures achieve  $11 \times$  lower memory on FPGAs [46].

## 5. Conclusions

We introduced EMMA, a physics-informed multimodal framework that recovers dynamical parameters directly from raw video, audio, and images. By coupling an LTC-based estimator with invariant calibration and cross-modal alignment, EMMA infers both explicit system parameters and implicit dynamical components that are not directly sensed, then uses them to reproduce observed trajectories with high fidelity. The recovered parameters are interpretable and executable, enabling simulation, verification, and downstream control without bespoke postprocessing. Across diverse canonical systems and real platforms, EMMA delivers accurate parameter recovery with a compact pipeline that uses standard sensors and off-the-shelf tooling. We expect EMMA to provide a strong foundation for learning physical models from opportunistic multimodal data and for building physical AI agents.

**Limitations** include dependence on at least one temporally varying modality, a linear frequency-speed audio prior that may degrade under turbulence, sensitivity to severe camera shake, and higher runtime from LTC-based ODE integration.

## Acknowledgments

This project is partially funded by DARPA AMP-N6600120C4020, DARPA FIRE-P000050426, NSF FDT-Biotech grant (2436801), NIH R21 grant (1R21HL175632).

## References

- [1] Martin Asenov, Michael Burke, Daniel Angelov, Todor Davchev, Kartic Subr, and Subramanian Ramamoorthy. Vid2param: Modeling of dynamics parameters from video. *IEEE Robotics and Automation Letters*, 5(2):414–421, 2020.
- [2] Ayan Banerjee and Sandeep K.S. Gupta. Recovering implicit physics model under real-world constraints. In *Proceedings of the 27th European Conference on Artificial Intelligence (ECAI)*, 2024.
- [3] Ayan Banerjee and Sandeep K.S. Gupta. EMILY: Extracting sparse model from ImpLicit dYnamics. In *ML-DE Workshop at ECAI*, pages 1–11, 2024.
- [4] Ayan Banerjee, Aranyak Maity, Imane Lamrani, and Sandeep K. S. Gupta. Towards certified safe personalization in learning-enabled human-in-the-loop human-in-the-plant systems. *J. Emerg. Technol. Comput. Syst.*, 22(1), 2025.
- [5] Giovanni Boschetti and Teresa Sinico. Designing digital twins of robots using simscape multibody. *Robotics*, 13(4): 62, 2024.
- [6] Gary Bradski. The opencv library. *Dr. Dobb's Journal of Software Tools*, 2000. OpenCV v4.6 used in this work.
- [7] Steven L Brunton, Joshua L Proctor, and J Nathan Kutz. Discovering governing equations from data by sparse identification of nonlinear dynamical systems. *Proceedings of the National Academy of Sciences*, 113(15):3932–3937, 2016.
- [8] Nikola Bulatovic and Slobodan Djukanovic. An approach to improving sound-based vehicle speed estimation. *arXiv preprint arXiv:2204.05082*, 2022.
- [9] Nikola Bulatovic and Slobodan Djukanovic. Mel-spectrogram features for acoustic vehicle detection and speed estimation. *arXiv preprint arXiv:2204.04013*, 2022.
- [10] Alejandro Castañeda Garcia, Jan Warchocki, Jan van Gemert, Daan Brinks, and Nergis Tömen. Learning physics from video: Unsupervised physical parameter estimation for continuous dynamical systems. In *IEEE/CVF Conference on Computer Vision and Pattern Recognition (CVPR)*, 2025.
- [11] Ricky T. Q. Chen, Yulia Rubanova, Jesse Bettencourt, and David Duvenaud. Neural ordinary differential equations. In *Advances in Neural Information Processing Systems (NeurIPS)*, 2018.
- [12] Wen-Hua Chen, Jun Yang, Lei Guo, and Shihua Li. Disturbance-observer-based control and related methods—an overview. *IEEE Transactions on Industrial Electronics*, 63(2):1083–1095, 2016.
- [13] George Cybenko. Approximation by superpositions of a sigmoidal function. *Mathematics of Control, Signals and Systems*, 2(4):303–314, 1989.
- [14] Claudio Dalla Man, Robert A. Rizza, and Claudio Cobelli. Meal simulation model of the glucose–insulin system. *IEEE Transactions on Biomedical Engineering*, 54(10): 1740–1749, 2007.
- [15] Edward De Brouwer, Jaak Simm, Adam Arany, and Yves Moreau. GRU-ODE-Bayes: Continuous modeling of sporadically-observed time series. In *Advances in Neural Information Processing Systems (NeurIPS)*, 2019.
- [16] Brian M. de Silva, Kathleen Champion, Markus Quade, Jean-Christophe Loiseau, J. Nathan Kutz, and Steven L. Brunton. Pysindy: A python package for the sparse identification of nonlinear dynamical systems from data. *Journal of Open Source Software*, 5(49):2104, 2020.
- [17] Ramin Hasani, Mathias Lechner, Alexander Amini, Daniela Rus, and Radu Grosu. Liquid time-constant networks. In *Proceedings of the AAAI Conference on Artificial Intelligence*, pages 7657–7666, 2021.
- [18] Florian Hofherr, Lukas Koestler, Florian Bernard, and Daniel Cremers. Neural implicit representations for physical parameter inference from a single video. In *Proceedings of the IEEE/CVF Winter Conference on Applications of Computer Vision*, pages 2093–2103, 2023.
- [19] Kurt Hornik, Maxwell Stinchcombe, and Halbert White. Multilayer feedforward networks are universal approximators. *Neural Networks*, 2(5):359–366, 1989.
- [20] S. M. Mostaq Hossain, Sohag Kumar Saha, Shampa Banik, and Trapa Banik. A new era of mobility: Exploring digital twin applications in autonomous vehicular systems. *arXiv preprint arXiv:2305.16158*, 2023.
- [21] Miguel Jaques, Michael Burke, and Timothy Hospedales. Physics-as-inverse-graphics: Unsupervised physical parameter estimation from video. In *International Conference on Learning Representations*, 2020.
- [22] Krishna Murthy Jatavallabhula, Miles Macklin, Florian Golemo, Vikram Voleti, Linda Petrini, Martin Weiss, Brendan Considine, Jerome Parent-Levesque, Kevin Xie, Kenny Erleben, Liam Paull, Florian Shkurti, Derek Nowrouzezahrai, and Sanja Fidler. gradsim: Differentiable simulation for system identification and visuomotor control. In *International Conference on Learning Representations (ICLR)*, 2021.
- [23] Glenn Jocher and Ultralytics. Yolo11. <https://github.com/orgs/ultralytics/discussions/16603>, 2024. Ultralytics announcement and docs.
- [24] Kadierdan Kaheman, Alan A. Kaptanoglu, Zachary G. Nicolaou, Kathleen Champion, Steven L. Brunton, and J. Nathan Kutz. Sindy-pi: A robust algorithm for parallel implicit sparse identification of nonlinear dynamics. *Proceedings of the Royal Society A*, 476(2242):20200279, 2020.
- [25] Jari Kaipio and Erkki Somersalo. *Statistical and Computational Inverse Problems*. Springer, New York, 2006.
- [26] Navami Kairanda, Edith Tretschk, Mohamed Elgharib, Christian Theobalt, and Vladislav Golyanik.  $\phi$ -sft: Shape-from-template with a physics-based deformation model. In *Proceedings of the IEEE/CVF Conference on Computer Vision and Pattern Recognition (CVPR)*, pages 3948–3958, 2022.
- [27] Eurika Kaiser, J. Nathan Kutz, and Steven L. Brunton. Sparse identification of nonlinear dynamics with control (sindyc). *IFAC-PapersOnLine*, 51(2):710–715, 2018.

- [28] Rudolf E. Kalman. A new approach to linear filtering and prediction problems. *Journal of Basic Engineering*, 82(1): 35–45, 1960.
- [29] Rama Kandukuri, Jan Achterhold, Michael Moeller, and Joerg Stueckler. Learning to identify physical parameters from video using differentiable physics. In *DAGM German Conference on Pattern Recognition*, pages 44–57. Springer, 2020.
- [30] Rama Krishna Kandukuri, Jan Achterhold, Michael Möller, and Jörg Stückler. Physical representation learning and parameter identification from video using differentiable physics. *International Journal of Computer Vision*, 130(1): 3–16, 2022.
- [31] J. Nathan Kutz, Steven L. Brunton, and Joshua L. Proctor. *Dynamic Mode Decomposition: Data-Driven Modeling of Complex Systems*. SIAM, 2016.
- [32] Ilya Loshchilov and Frank Hutter. Sgdr: Stochastic gradient descent with warm restarts. In *International Conference on Learning Representations (ICLR)*, 2017.
- [33] Ilya Loshchilov and Frank Hutter. Decoupled weight decay regularization. In *International Conference on Learning Representations (ICLR)*, 2019.
- [34] Pingchuan Ma, Tao Du, Joshua B. Tenenbaum, Wojciech Matusik, and Chuang Gan. Risp: Rendering-invariant state predictor with differentiable simulation and rendering for cross-domain parameter estimation. In *International Conference on Learning Representations (ICLR)*, 2022.
- [35] F. Marin, A. Rohatgi, and S. Charlot. Webplotdigitizer: a polyvalent and free software to extract spectra from old astronomical publications. arXiv:1708.02025, 2017.
- [36] Brian McFee, Colin Raffel, Dawen Liang, Daniel P. W. Ellis, Matt McVicar, Eric Battenberg, and Oriol Nieto. librosa: Audio and music signal analysis in python. In *Proc. 14th Python in Science Conference*, pages 18–25, 2015.
- [37] Raul Mur-Artal and J. D. Tardós. ORB-SLAM2: An open-source SLAM system for monocular, stereo, and RGB-D cameras. *IEEE Transactions on Robotics*, 33(5):1255–1262, 2017.
- [38] Sam Nazari. The unknown input observer and its advantages with examples. *arXiv preprint arXiv:1504.07300*, 2015.
- [39] Adam Paszke, Sam Gross, Francisco Massa, Adam Lerer, James Bradbury, Gregory Chanan, Trevor Killeen, Zeming Lin, Natalia Gimelshein, Luca Antiga, Alban Desmaison, Andreas Kopf, Edward Yang, Zachary DeVito, Martin Raison, Alykhan Tejani, Sasank Chilamkurthy, Benoit Steiner, Lu Fang, Junjie Bai, and Soumith Chintala. Pytorch: An imperative style, high-performance deep learning library. In *Advances in Neural Information Processing Systems (NeurIPS)*, 2019.
- [40] Joshua L. Proctor, Steven L. Brunton, and J. Nathan Kutz. Dynamic mode decomposition with control. *SIAM Journal on Applied Dynamical Systems*, 15(1):142–161, 2016.
- [41] Maziar Raissi, Paris Perdikaris, and George E. Karniadakis. Physics-informed neural networks: A deep learning framework for solving forward and inverse problems involving nonlinear partial differential equations. *Journal of Computational Physics*, 378:686–707, 2019.
- [42] Peter J. Schmid. Dynamic mode decomposition of numerical and experimental data. *Journal of Fluid Mechanics*, 656:5–28, 2010.
- [43] Albert Tarantola. *Inverse Problem Theory and Methods for Model Parameter Estimation*. SIAM, Philadelphia, PA, 2005.
- [44] Kui Wang, Tao Yu, Zongdian Li, Kei Sakaguchi, Omar Hashash, and Walid Saad. Digital twins for autonomous driving: A comprehensive implementation and demonstration. *arXiv preprint arXiv:2401.08653*, 2024.
- [45] Matthew O. Williams, Ioannis G. Kevrekidis, and Clarence W. Rowley. A data-driven approximation of the koopman operator: Extended dynamic mode decomposition. *Journal of Nonlinear Science*, 25(6):1307–1346, 2015.
- [46] Bin Xu, Ayan Banerjee, and Sandeep K.S. Gupta. Model recovery at the edge under resource constraints for physical AI. *arXiv preprint arXiv:2512.02283*, 2025.
- [47] Zulko and contributors. Moviepy: Python module for video editing. <https://zulko.github.io/moviepy/>, 2025. Version used in this work.

# EMMA: Extracting Multiple physical parameters from Multimodal Data

## Supplementary Material

### S1. Ablation Study

This supplement expands on the architecture behind EMMA’s multi-modal, physics-informed estimator by isolating the impact of (i) forcing inputs and audio wavelength, (ii) the LTC network vs. alternative sequence models, (iii) implicit dynamics, and (iv) invariant knowledge. We follow the same dynamical systems introduced in the main paper (pendulum), and the real-world rover cases with hidden inputs. See the architecture and training details in the main paper (Fig. 2; Secs. 3-4). *Where not stated otherwise, the loss and simulator are identical to the main setup.*

#### S1.1. Case Study with No Forcing Input (Pendulum)

##### S1.1.1. LTC Architecture: Pendulum

**Setup.** We ablated the LTC-NN using three alternative recurrent architectures (LSTM, GRU, and Transformer) as they share similar sequential structure. The pendulum example estimates two parameters and has no external force input  $u(t)$ , making it less complex.

Architecture	45 cm	90 cm	150 cm
LSTM	0.49±0.20	0.98±0.41	1.35±0.69
GRU	0.49±0.20	0.98±0.41	1.35±0.69
Transformer	0.49±0.20	1.07±0.42	1.35±0.69
<b>LTC</b>	0.49±0.20	0.98±0.41	1.35±0.69
Ground Truth $L$ (m)	0.45	0.90	1.50

(a) Estimated length  $L$  (m)

Architecture	45 cm	90 cm	150 cm
LSTM	0.054±0.023	0.054±0.023	0.045±0.023
GRU	0.054±0.023	0.054±0.023	0.045±0.023
Transformer	0.054±0.023	0.053±0.021	0.045±0.023
<b>LTC</b>	0.054±0.023	0.054±0.023	0.045±0.023
Ground Truth	0.05	0.05	0.05

(b) Damping time-constant  $\tau$  (1/s)

Table S1. Comparison of different architectures using the Pendulum (no forcing) example.

From the results in Table S1, all architectures estimate very similar parameters with comparable accuracy, making our EMMA structure robust and versatile. This confirms that irrespective of architecture, EMMA is efficient on less complex examples with no force input.

#### S1.2. Case Study with Forcing Input

##### S1.2.1. LTC Architecture: Rover

**Setup.** The motivation and justification for using LTC-NN arises when we have a forcing input  $u(t)$  and a more

complex example. We used the same three alternative architectures as for the pendulum but on the more complex Rover example, which has multiple parameters to estimate along with external force.

Parameters	GT	LTC (Ours)	GRU	LSTM	Transformer
X-arm length $m$	0.178	<b>0.173</b>	0.202	0.168	0.169
Y-arm length $m$	0.144	<b>0.133</b>	0.195	0.174	0.197
Mass $kg$	26.88	<b>27.79</b>	39.50	39.45	39.28
CoM height $m$	0.112	<b>0.119</b>	0.108	0.123	0.094
Wheel radius $r$	0.201	<b>0.205</b>	0.196	0.212	0.188
Convergence epoch	–	5	10	14	54
Training time/epoch	–	63.57s	22.36	25.07	62.82

Table S2. Comparison of different architectures using the Rover (forced dynamics).

The results in Table S2 show that the accuracy of other architectures degrades compared to LTC-NN on the more complex forced dynamics example. LTC-NN is therefore the most suitable architecture choice for EMMA, yielding accurate results with faster convergence.

##### S1.2.2. Multi-modal Ablation Without Audio

**Setup.** The use of multi-modal input is one of our key contributions, where we extract knowledge from different modalities making EMMA useful for various scenarios. We performed an ablation study on the rover example with video and audio input and compared it against video-only input. The setup was identical except the audio knowledge was removed.

Parameters	GT	Video+Audio	Video-only
X-arm length ( $m$ )	0.178	0.163	0.189
Y-arm length ( $m$ )	0.144	0.133	0.203
Mass ( $kg$ )	26.88	27.79	39.64
CoM height ( $m$ )	0.112	0.129	0.108
Wheel radius ( $r$ )	0.201	0.245	0.171
Convergence epoch	–	5	30
Training time (s)	–	54.1	122.3

Table S3. Effect of audio on parameter recovery under forced dynamics.

Table S3 clearly demonstrates the importance of audio knowledge in parameter estimation. When more modalities are available, EMMA can observe and incorporate knowledge that better guides the model to estimate accurate parameters in less time.

## S2. Physics Equations

We collect the governing equations for all systems used in the ablations, with parameters and units. These mirror the forms used in the simulator head of EMMA.

### S2.1. Damped Pendulum

For a pendulum with angle  $\theta$ , angular velocity  $\omega = \dot{\theta}$ , the dynamics follow:

$$\frac{d\theta}{dt} = \omega. \quad (\text{S1})$$

$$\frac{d\omega}{dt} = -\frac{g}{L} \sin \theta - \frac{\tau}{L} \omega. \quad (\text{S2})$$

**Parameters:**  $L \in (0.1, 2.0]$  m (length),  $\tau \in (0, 0.5]$  s<sup>-1</sup> (damping coefficient),  $g = 9.81$  m/s<sup>2</sup> (gravity).

### S2.2. Torricelli Drainage

For fluid draining through an orifice, height  $h(t)$  evolves as:

$$\frac{dh}{dt} = -K\sqrt{h}, \quad K = C_d A_{\text{orifice}} \sqrt{2g} / A_{\text{tank}}. \quad (\text{S3})$$

**Parameters:**  $K \in (0.001, 0.1]$   $\sqrt{\text{m}}/\text{s}$  (drainage coefficient).

### S2.3. LED Exponential Decay

Light intensity  $I(t)$  follows first-order decay:

$$\frac{dI}{dt} = -\gamma I(t), \quad I(t) = I_0 e^{-\gamma t}. \quad (\text{S4})$$

**Parameters:**  $\gamma \in (0.01, 5.0]$  s<sup>-1</sup> (decay rate).

### S2.4. Sliding Block with Friction

Block on inclined plane with velocity  $v$ :

$$\frac{dv}{dt} = g \sin(\alpha) - \mu g \cos(\alpha). \quad (\text{S5})$$

**Parameters:**  $\alpha \in [10^\circ, 45^\circ]$  (incline),  $\mu \in [0.1, 0.5]$  (friction).

### S2.5. Free Fall

Vertical velocity  $v$  under quadratic drag:

$$\frac{dv}{dt} = g - kv^2 \text{sign}(v). \quad (\text{S6})$$

**Parameters:**  $k = \frac{C_d \rho A}{2m}$  (drag coefficient).

### S2.6. Differential-Drive Rover (9 Parameters)

The rover combines kinematic constraints with dynamic forces:

$$v = \frac{r(\omega_r + \omega_l)}{2}, \quad \dot{\psi} = \frac{r(\omega_r - \omega_l)}{W}. \quad (\text{S7})$$

$$m\dot{v}_x = F_{\text{motor}} - F_{\text{friction}} - F_{\text{drag}}. \quad (\text{S8})$$

**Measured Parameters:**  $a = 0.178$  m (X-arm),  $b = 0.144$  m (Y-arm),  $r = 0.201$  m (wheel radius),  $m = 26.88$  kg,  $W = 0.32$  m (wheelbase).

**Implicit Parameters:**  $k_f = 0.15$  (friction),  $C_d = 0.42$  (drag),  $C_M = 0.112$  m (CoM height).

### S2.7. 6-DOF Quadrotor (12 Parameters)

Full rigid-body dynamics with rotor dynamics:

$$\tau^2 \ddot{w}_i + 2\zeta \tau \dot{w}_i + w_i = k_p u_i. \quad (\text{S9})$$

$$T_i = k_{T_h} w_i^2, \quad \tau_i = k_{T_o} w_i^2. \quad (\text{S10})$$

$$m\ddot{\mathbf{p}} = R(\mathbf{q})\mathbf{T} - mg\mathbf{e}_z - \mathbf{F}_{\text{drag}}. \quad (\text{S11})$$

**Measured Parameters:**  $k_{T_h} = 1.1 \times 10^{-5}$  N·s<sup>2</sup>/rad<sup>2</sup>,  $k_{T_o} = 1.3 \times 10^{-7}$  N·m·s<sup>2</sup>/rad<sup>2</sup>,  $d_{x_m} = 0.18$  m,  $d_{y_m} = 0.20$  m,  $d_{z_m} = 0.07$  m.

**Audio-Inferred:**  $k_p = 0.91$ ,  $\tau = 0.012$  s,  $\zeta = 0.7$ .

### S3. Differentiable Trajectory Rollout

To ensure numerical stability and consistency with the architecture layout in Fig. 2 of the main paper, we employ a differentiable 4th-order Runge-Kutta (RK4) integrator. This provides higher-order error control compared to standard Euler integration, which is critical for stiff dynamical systems like the quadrotor.

Given estimated parameters  $\hat{\theta}$  from the LTC network and the continuous physics function  $\mathbf{f}$ , the state update from time  $t$  to  $t + 1$  is computed as:

$$k_1 = f(x_t, u_t; \hat{\theta}). \quad (\text{S12})$$

$$k_2 = f\left(x_t + \frac{\Delta t}{2} k_1, u_{t+\frac{1}{2}}; \hat{\theta}\right). \quad (\text{S13})$$

$$k_3 = f\left(x_t + \frac{\Delta t}{2} k_2, u_{t+\frac{1}{2}}; \hat{\theta}\right). \quad (\text{S14})$$

$$k_4 = f(x_t + \Delta t k_3, u_{t+1}; \hat{\theta}). \quad (\text{S15})$$

$$x_{t+1} = x_t + \frac{\Delta t}{6} (k_1 + 2k_2 + 2k_3 + k_4). \quad (\text{S16})$$

where the simulation time step is clamped at  $\Delta t = \min(0.03, \text{fps}^{-1})$ . Intermediate control inputs  $u_{t+\frac{1}{2}}$  are obtained via linear interpolation of the forcing signal. The simulation runs for  $T_{\text{sim}} = \min(500, T)$  steps. Parameter physical constraints are enforced via soft clamping:  $\theta_i \leftarrow \max(\epsilon, \theta_i)$  with  $\epsilon = 10^{-4}$ .

### S4. Additional Robustness and Ablation Experiments

This section reports five additional experiments validating EMMA's robustness across feature extraction backbones, architecture choices, initialization sensitivity, statistical reproducibility, and audio noise levels.

#### S4.1. Optical Flow vs. YOLO (Detector Agnosticism)

To verify that EMMA's physics extraction is independent of the object detection front-end, we replaced YOLOv11

with unsupervised Farneback optical flow tracking on both the rover and pendulum systems. Table S4 shows that optical flow achieves comparable accuracy, confirming that EMMA’s core contribution lies in the LTC physics layer rather than the feature extractor.

(a) Rover			
Parameter	Ground Truth	YOLOv11	Optical Flow
$a$ (m)	0.178	0.196	<b>0.184</b>
$b$ (m)	0.144	<b>0.134</b>	0.110
$r$ (m)	0.201	0.223	<b>0.202</b>
(b) Pendulum ( $L, m$ )			
Configuration	Ground Truth	YOLOv11	Optical Flow
45 cm	0.45	<b>0.50±0.04</b>	0.66±0.00
90 cm	0.90	0.86±0.07	<b>0.89±0.00</b>
150 cm	1.50	<b>1.50±0.00</b>	1.49±0.00

Table S4. YOLOv11 vs. unsupervised optical flow on rover and pendulum. Optical flow achieves comparable accuracy without any pretrained detector. Best per row in bold.

### S4.2. Statistical Validation (Multi-Seed Reproducibility)

Table S5 reports rover parameter estimates over 5 random seeds (42–46), providing standard deviations that quantify reproducibility. Average error across four measurable parameters is  $9.5\% \pm 8.9\%$ .

Parameter	Ground Truth	Mean ± Std	Error (%)
$a$ (m)	0.178	0.184 ± 0.020	3.4
$b$ (m)	0.144	0.176 ± 0.031	22.2
$r$ (m)	0.201	0.222 ± 0.027	10.4
$CM$ (m)	0.112	0.114 ± 0.008	1.8

Table S5. Rover statistical validation over 5 random seeds (42–46).  $\pm$  denotes standard deviation across seeds.

### S4.3. Drone Statistical Validation (Multi-Seed Reproducibility)

Table S6 reports drone parameter estimates over 5 random seeds (42–46), providing standard deviations that quantify reproducibility. Average error across all measurable parameters is  $17.5\%$ .

Parameter	Ground Truth	Mean ± Std	Error (%)
$k_{Th}$	1.1	1.076 ± 0.000	2.2
$k_{To}$	1.3	1.632 ± 0.000	25.5
$k_p$	0.91	1.000 ± 0.000	9.9
$\tau_2$	0.012	0.015 ± 0.000	25.0
$d_{xm}$	0.18	0.160 ± 0.000	11.1
$d_{ym}$	0.20	0.160 ± 0.000	20.0
$d_{zm}$	0.07	0.050 ± 0.000	28.6

Table S6. Drone statistical validation over 5 random seeds (42–46).  $\pm$  denotes standard deviation across seeds.

### S4.4. LTC vs. Neural ODE vs. CT-GRU

We compare LTC against two continuous-time alternatives: Neural ODE and CT-GRU. Table S7 shows that all architectures perform comparably on the unforced pendulum. Under forcing inputs (rover), LTC outperforms Neural ODE by approximately 25% and CT-GRU by approximately 5% in average parameter error, validating that input-dependent time constants are critical for modeling forced dynamics.

(a) Rover (Forcing Input)				
Parameter	Ground Truth	LTC	Neural ODE	CT-GRU
$a$ (m)	0.178	0.196	0.238	<b>0.179</b>
$b$ (m)	0.144	<b>0.134</b>	0.212	0.186
$r$ (m)	0.201	<b>0.223</b>	0.244	0.226
Avg. Error		<b>9.3%</b>	34.1%	14.1%
(b) Pendulum (No Forcing)				
Configuration	Ground Truth	LTC	Neural ODE	CT-GRU
45 cm	0.45	<b>0.50</b>	0.59	0.54
90 cm	0.90	0.86	0.99	<b>0.94</b>
150 cm	1.50	<b>1.50</b>	1.56	1.48
Avg. Error		<b>5.2%</b>	15.0%	8.6%

Table S7. Continuous-time architecture comparison. All architectures perform comparably without forcing; under forcing inputs, LTC outperforms Neural ODE by approximately 25% and CT-GRU by approximately 5%. Best per row in bold.

### S4.5. Initialization Sensitivity

To evaluate robustness to poor initialization, we expand parameter bounds by 200% and initialize far from ground truth. Table S8 shows EMMA achieves  $<10\%$  error in 5 out of 6 configurations, confirming that accurate estimation does not require initialization close to ground truth.

(a) Sliding Block ( $\alpha$ )				
Config	GT	Init	Est	Error (%)
Low	20°	25°	20.69°	<b>3.45</b>
Mid	25°	30°	25.48°	<b>1.92</b>
High	30°	45°	28.25°	<b>5.84</b>
(b) Pendulum ( $L, m$ )				
Config	GT	Init	Est	Error (%)
45 cm	0.45	0.85	0.447	<b>0.73</b>
90 cm	0.90	1.30	0.683	24.08
150 cm	1.50	1.10	1.620	<b>8.02</b>

Table S8. Initialization sensitivity with 200% expanded bounds and distant initialization. Bold indicates  $<10\%$  error. EMMA converges accurately in 5 of 6 configurations.

### S4.6. Audio Noise Robustness

We inject additive Gaussian noise at SNR levels of 20, 10, and 5 dB into the rover audio stream. Table S9 shows that parameter estimates vary by less than 1.1% across all noise

levels, demonstrating that EMMA’s audio pipeline degrades gracefully under realistic acoustic interference.

Parameter	Ground Truth	SNR 20 dB	SNR 10 dB	SNR 5 dB	Var (%)
$a$ (m)	0.178	0.205	0.205	0.205	0.15
$b$ (m)	0.144	0.165	0.165	0.165	0.55
$r$ (m)	0.201	0.184	0.186	0.186	1.08
$CM$ (m)	0.112	0.115	0.115	0.115	0.04

Table S9. Rover audio noise robustness. Additive Gaussian noise at three SNR levels causes <1.1% variation in all estimated parameters.